1
2
3
4

# Stress Changes on the Garlock Fault During and After the 2019 Ridgecrest Earthquake Sequence

5     1.  **Marlon D. Ramos**[1]      ramosmd@umich.edu
6     2.  **Jing Ci Neo**[1]          neoj@umich.edu
7     3.  **Prithvi Thakur**[1]       prith@umich.edu
8     4.  **Yihe Huang**[1]           yiheh@umich.edu
9     5.  **Shengji Wei**[2]          shjwei@ntu.edu.sg

10
11
12    1. University of Michigan, Department of Earth and Environmental Sciences
13    2. Nanyang Technological University of Singapore, Asian School of the Environment

14
15
16
17
18
19
20
21
22
23
24
25
26
27
28
29
30
31
32
33
34
35
36
37
38
39
40
41
42
43
44
45
46

47 **Abstract**

48     The recent 2019 Ridgecrest earthquake sequence in Southern California jostled the

49 seismological community by revealing a complex and cascading foreshock series that culminated

50 in a M7.1 mainshock. But the central Garlock fault, despite being located immediately south of

51 this sequence, did not coseismically fail. Instead, the Garlock fault underwent post-seismic creep

52 and exhibited a sizeable earthquake swarm. The dynamic details of the rupture process during the

53 mainshock is largely unknown, as is the amount of stress needed to bring the Garlock fault to

54 failure. We present an integrated view of how stresses changed on the Garlock fault during and

55 after the mainshock using a combination of tools including kinematic slip inversion, Coulomb

56 stress change, and dynamic rupture modeling. We show that positive Coulomb stress changes

57 cannot easily explain observed aftershock patterns on the Garlock fault, but are consistent with

58 where creep was documented on the central Garlock fault section. Our dynamic model is able to

59 reproduce the main slip asperities and kinematically estimated rupture speeds ($\leq$ 2 km/s) during

60 the mainshock, and suggests the temporal changes in normal and shear stress on the Garlock fault

61 were greatest near the end of rupture. The largest static and dynamic stress changes on the Garlock

62 fault we observe from our models coincide with the creeping region, suggesting that positive stress

63 perturbations could have caused this during or after the mainshock rupture. This analysis of near-

64 field stress change evolution gives insight into how the Ridgecrest sequence influenced the local

65 stress field of the northernmost Eastern California Shear Zone.

66 **Introduction**

67     The 2019 Ridgecrest earthquake sequence involved the rupture of a left-lateral M6.4

68 foreshock that occurred on July 4, and a right-lateral M7.1 mainshock that occurred on July 6 and

69 initiated approximately 13 km northwest of the foreshock epicenter (Fig. 1a). This sequence was

70 characterized by the activation of multiple orthogonal fault segments that are collectively referred

71 to as the Little Lake fault zone (Llfz). Coseismic rupture of these faults continues to produce

72 aftershocks, but it did not influence the adjacent left-lateral Garlock fault to fail. Instead, this

73 sequence caused as much as three centimeters of surface creep on the Garlock fault that has been

74 detected geodetically (Barnhart et al., 2019; Ross et al., 2019).

75     Several kinematic slip models have been developed to estimate the evolution of slip and

76 rupture propagation during this highly complex sequence (Barnhart et al., 2019; Chen et al., 2020;

77 Goldberg et al., 2020; Liu et al., 2019; Ross et al., 2019; Zhang et al., 2020). These models are

78    consistent in the respect that a majority of foreshock and mainshock slip is limited to the upper 10
79    km depth. Positive stress change amplitudes (~0.5 MPa) are suggested from static Coulomb
80    modeling generally coincide with the ~25-km long region of creep on the central Garlock fault
81    segment (Barnhart et al., 2019). But the dynamic details of rupture and how stresses were mediated
82    by the seismic wavefield remains hazy. The Garlock fault was apparently not near critical failure,
83    or else we would have observed coseismic rupture there as well; this implies that the stress
84    perturbations were unable to bring shear stresses to overcome the static Garlock fault strength.

85         When the Garlock fault will slip again is a major unknown. The Garlock fault extends for
86    ~260 km and is geometrically segmented into western, central, and eastern sections that are
87    characterized by variations in geologic slip-rate and recurrence interval (Davis and Burchfiel,
88    1973; Hill et al., 1953, McGill and Sieh, 1991). Astiz and Allen (1983) analyzed historical
89    seismicity on this fault and hypothesized that a rupture on the eastern Garlock segment may be
90    more likely given its apparent seismic gap, though both the central and western sections can
91    independently support ~M7 earthquakes. Paleoseismic evidence suggests historic, non-periodic
92    surface rupture for the central Garlock segment (Dawson et al., 2003). During the Ridgecrest
93    sequence, different regions of the central Garlock fault segment experienced a swarm of low-
94    magnitude earthquakes (ML<3.2; Ross et al., 2019) and underwent creep. How the strain
95    accumulation budget of the central Garlock fault was influenced by the recent Ridgecrest sequence
96    is enigmatic and warrants further scrutiny for seismic hazard analysis. A spatial separation between
97    the Ridgecrest mainshock and Garlock fault planes is furthermore subject to uncertainty, as is the
98    possibility of rupture branching from a segment of the Garlock fault onto an adjacent segment or
99    to the San Andreas fault during a future earthquake. In particular, the central and western segments
100    have co-ruptured within the last 10 kya, despite a step-over structure in between them (Madugo et
101    al., 2012). Assessing the possibility of how close the Garlock fault is to failure depends on both
102    the static and dynamic stress perturbations from the Ridgecrest sequence.

103         We aim to present a physically consistent picture of the stress interaction vis-à-vis the
104    Garlock fault during and after the Ridgecrest sequence. We draw from updated kinematic
105    inversion results that utilize geodetic, teleseismic and near-field strong ground-motion recordings
106    to independently constrain the fault slip amplitude, extent and rupture initiation locations of the
107    foreshocks and M7.1 mainshock. This is then used to inform our static Coulomb stress analysis
108    and dynamic rupture modeling efforts. Our analysis illustrates that both normal and shear stress

109 changes were highest on the Garlock fault at the end of mainshock rupture, and could have been

110 responsible for the observed geodetic creep as soon as ~30 seconds from mainshock rupture

111 initiation.

112 **Methodology**

113 *Kinematic Slip Inversion*

114       We use a joint slip-inversion model that is based on static GPS, teleseismic and local

115 strong-ground motion datasets (Ji et al., 2002). The M6.4 foreshock and the M7.1 mainshock are

116 modeled with two and single fault plane geometries, respectively (Fig. 1). Slip along the

117 mainshock fault occurs along a 100-km long segment that dips at ~88 degrees (Fig. 1b). Of the

118 two foreshock fault planes, one is nearly parallel to the strike of the mainshock (Plane 1), whereas

119 the second is perpendicular to the mainshock (Plane 2; Fig. 1c, Table 1). These fault plane

120 geometries are consistent with those estimated by the USGS and do not extend deeper than 16-km

121 depth. Geologic mapping and Interferometric Synthetic Aperture Radar (InSAR) observations of

122 surface-breaching rupture strands during the Ridgecrest sequence suggest that our geometries are

123 reasonable (Kendrick et al., 2019; Xu et al., 2020). We use the slip inversion results for the

124 foreshock and mainshock fault planes as input into our static and dynamic stress change modeling.

125 *Static Model: Coulomb Stress-Change*

126       Static stress changes are the final changes in the normal and shear stresses on the fault in

127 response to slip after all seismic waves have propagated through. Such stress changes during the

128 foreshock and mainshock of the Ridgecrest sequence have triggered thousands of aftershocks

129 (Ross et al., 2019). Coseismic stress changes have also been known to enhance or to reduce creep

130 after the earthquake (e.g., Allen et al., 1972, Bodin et al., 1994, Lienkaemper et al., 1997). Barnhart

131 et al. (2019) observed that an increase in the Coulomb stress change from the Ridgecrest

132 earthquake was correlated with the surface deformation after the earthquake. Studies have also

133 suggested that the M6.4 foreshock and other large foreshocks promoted the rupture of the

134 mainshock (Barnhart et al., 2019; Goldberg et al., 2020; Lozos and Harris, 2020).

135       To assess static stress changes, we calculate the Coulomb stress change ($\Delta CFS$) using the

136 Coulomb3 software (Lin and Stein 2004; Toda et al. 2005). We investigate the $\Delta CFS$ caused by

137 the foreshock on the mainshock and separate the contribution of stress change from each of the

138 two foreshock fault planes (Plane 1 and Plane 2; Fig 2). We use a friction coefficient of 0.6 and a

139  depth of 5 km for the foreshock-mainshock static stress change calculation because a majority of
140  slip is resolved on foreshock Plane 2 (Fig. 1c), which will dominate the $\Delta CFS$ amplitude.

141  We also calculate the $\Delta CFS$ due to mainshock slip on the Garlock fault. We represent the
142  Garlock fault geometry as a plane with a strike, dip and rake of 70, 90, and 0 degrees, respectively.
143  The strike of the Garlock fault varies from 68° in the east to 84° in the west (Fig. 3), but we use
144  70° for the receiver fault as it is closest to the strike of the western Garlock fault segment where
145  the cluster of aftershocks occurred. Lastly, to address uncertainty in static friction level and
146  hypocenter depth, we also examine how varying these parameters influences our results. We
147  compare the results from friction coefficients of 0.2, 0.4 and 0.6, and at 5 km depth, where peak
148  slip occurred, and at 10 km depth, where the asperity with most slip extends.

149  *Dynamic Model: Initial Conditions and Constraints*

150  We model the mainshock fault plane as a 100-km, planar 2-D crack embedded in a
151  homogeneous, isotropic, and linearly elastic medium with a shear-wave speed of 3.2 km/s. The
152  model domain is composed of rectangular elements enclosed on all sides by absorbing boundaries
153  (Fig. S1). We choose a finite element size of 600-m with four Gauss-Lobatto-Legendre nodes
154  (NGLL) to resolve dynamic rupture propagation at seismic frequencies up to 1 Hz for consistency
155  with that resolved by the strong-motion dataset.

156  We select the linear slip-weakening friction law to control fault slip evolution and utilize
157  the 2-D spectral element code SEM2DPACK to solve for dynamic rupture propagation (Ampuero,
158  2009). The critical-slip distance ($D_c$) is 0.3 m, which is constant along the fault (except for ~15 km
159  around the nucleation region) and is within the plausible range of previous slip-weakening
160  dynamic rupture simulations for other crustal earthquakes of comparable magnitude and rupture
161  dimension (e.g., Ma and Archuleta, 2006; Lozos and Harris, 2020; Tinti et al., 2009). If dynamic
162  friction ($\mu_d$) is below the static friction ($\mu_s$) level, then the fault experiences a strength-drop during
163  coseismic rupture and its frictional behavior is slip-weakening; conversely, if the dynamic friction
164  is greater than static friction, there is no work available to grow the propagating shear crack and
165  the frictional behavior is slip-strengthening. The static friction coefficient is 0.5 everywhere along
166  the fault. The fault is slip-weakening ($\mu_d = 0.1$) along the central 70 km segment (35 km southeast
167  and northwest of hypocenter) and slip-strengthening ($\mu_d = 0.7$) everywhere else in order to prohibit
168  rupture from breaking the entire fault.

169    Given that we represent a strike-slip fault as a Mode II in-plane crack, our stress and friction

170 conditions are relative to a region on the mainshock fault plane at depth. Our model aims to

171 reproduce the rupture propagation along the section of the fault that crosses through the main slip

172 asperity imaged in the kinematic inversion (Fig. 4). Effective normal stress is set to a constant

173 level of 50 MPa that is consistent with elevated pore-pressure levels in the middle of permeable

174 fault zones (Rice, 1992).

175    The initial shear stress distribution is a critical ingredient for any dynamic earthquake

176 rupture model and determines the dynamic stress drop which in turn governs slip amplitude. We

177 first calculate the static stress drop due to fault slip given by the kinematic inversion using a

178 computationally efficient algorithm (Fig. 4; Ripperger and Mai, 2004). Earthquakes can exhibit

179 total or near-total stress-drop due to strong dynamic weakening (e.g., Noda and Lapusta, 2013;

180 Brodsky et al., 2020), meaning that the final shear stress on the fault after an earthquake is at or

181 very near its dynamic fault strength level (the product of effective normal stress and dynamic

182 friction). We make this assumption to calculate our initial shear stress by adding the static stress

183 drop to the dynamic fault strength (Fig. 4).

184    Rupture is artificially nucleated in the middle of the fault using the time-weakening method

185 (Andrews, 1985). This technique requires twice the critical half-crack length ($2L_c$), an effective

186 friction level ($\mu_o$), and a weakening time scale ($T_c$) after which the prescribed nucleation is turned

187 off and rupture spontaneously evolves according to the non-linear interaction between fault

188 strengths and stresses. Given the friction law parameters we assume for Mode II rupture in an

189 elastic domain, $2L_c$ is given by

190
$$2L_c = \frac{2}{1-v}\frac{G}{\pi}\frac{\tau_s-\tau_d}{(\tau_o-\tau_d)^2}D_c \tag{1}$$

191    where G is the shear modulus (30 GPa), $v$ is the Poisson's ratio, $\tau_s$ is the static fault

192 strength, $\tau_d$ is the dynamic fault strength, $\tau_o$ is the initial shear stress, and $\mu_o$ is the effective

193 friction coefficient calculated as the ratio between initial shear and effective normal stress

194 amplitudes at the hypocenter. We determined that a $2L_c$ of 2 km ($\mu_o$ of ~0.1) and $T_c$ of 10 seconds

195 are necessary to nucleate and sustain spontaneous rupture.

196 **Results**
197 *Kinematic Slip Inversion*
198    Using our kinematic inversion methodology, the mainshock hypocenter has been relocated

199 to a depth of 3 km by the arrival times of nearby strong motion and broadband seismic stations

200  (Fig 1b). The aftershock hypocenter is deeper (9 km) and slip is distributed across two fault

201  segments (Fig 1c). The fault parameters and hypocenters of both earthquakes are summarized in

202  Table 1. We note that the M7.1 mainshock ruptured bilaterally with a majority of slip concentrated

203  within the upper 10 km and a peak slip amplitude of 4.7 m located ~10 km NW of the hypocenter

204  (Fig. 1b). There is a smaller asperity that underwent ~ 2.5 m of slip SE of the mainshock

205  hypocenter, as well. On the other hand, peak slip resolved for the foreshock is lower (1.3 m) and

206  occurred mostly on Plane 2, which is perpendicular to the mainshock fault plane (1c).

207  We also compare our mainshock slip inversion results to those from other studies of the

208  Ridgecrest mainshock. We utilize seismic and GPS datasets to constrain the slip which is similar

209  to the approach by Liu et al., (2019). In contrast, other studies make use of a combination of

210  seismic, high-rate GPS and InSAR (Chen et al., 2020; Goldberg et al., 2020; Ross et al., 2019),

211  InSAR and optimal image-tracking (Barnhart et al., 2019), or only seismic datasets (Zhang et al.,

212  2020). The details of slip distribution, and in particular the relative location and amplitude of

213  maximum slip, varies between studies. The maximum slip is mostly shallower (~4 km, Barnhart

214  et al., 2019), to the northwest of (~10 km, Liu et al., 2019), or slightly deeper (~5 km, Ross et al.,

215  2019) than the hypocenter location used in their inversion. The kinematic slip inversion we present

216  resolves two primary slip patches (i.e., Fig. 1), which have similar amplitudes (4.7 m and 2.5 m)

217  and locations (northwest and southeast of hypocenter) to the Barnhart et al., (2019), Liu et al.,

218  (2019), and Zhang et al., (2020) inversion results. A major difference in maximum slip amplitude

219  occurs between our model and the Ross et al., (2019) study, which estimates as much as nine

220  meters of slip between 5 and 10 km depth. Other notable changes between our study and other's

221  include a more widely distributed higher (> 4 m) slip distribution (Chen et al., 2020), or a

222  maximum slip amplitude difference on the order of 1.5 meters between what is resolved from our

223  inversion (4.7 m) and the Goldberg et al., (2020) [~3.5 m] study. Such differences are most likely

224  due the datasets used to constrain the inversions as well as the particular inversion

225  parameterization. Overall, our mainshock slip distribution is consistent with other published

226  models, characterized by bilateral rupture propagation and a shallow (< 10 km) slip distribution.

227  *Static Stress Change*

228  We find the foreshock increased the $\Delta CFS$ near the edges of the foreshock faults, especially

229  at the intersection of Plane 2 and mainshock fault, but our relocated mainshock hypocenter is

230  located in a region of slightly decreased $\Delta CFS$ (Fig. 2a, S2). However, this result depends on the

7

231 method used to locate the mainshock hypocenter and its uncertainty. For instance, the Advanced

232 National Seismic System Comprehensive Catalog (ANSS) epicentral coordinates agree with ours

233 to within a kilometer but its depth is 5 km deeper than our preferred depth of 3 km, whereas the

234 hypocenter resolved by Ross et al. (2019) is ~12 km away from the foreshock hypocenter but at a

235 similar shallow depth (< 4 km). The hypocenters estimated by the ANSS catalog and by Ross et

236 al. (2019) are located near the edges of different regions of positive $\Delta CFS$. We also calculated the

237 $\Delta CFS$ from both foreshock planes separately (Fig. 2b, c). Plane 2 has a much larger slip compared

238 to Plane 1, with almost twice the peak slip (i.e., 1.3 versus 0.74 m; Table 1). However, Plane 1

239 causes a ~0.5 MPa greater $\Delta CFS$ on the southeast region of the mainshock fault compared to Plane

240 2, as Plane 1 is closer (Fig. 2b). This underscores the sensitivities of the $\Delta CFS$ to input fault slip

241 amplitude and extent.

242        We further calculate the $\Delta CFS$ on the Garlock fault due to mainshock slip and assess the

243 effect of various friction coefficients and depths on our results. Overall, we find that the friction

244 coefficient has a relatively small (i.e., a difference within ~ 0.1 MPa) impact on our $\Delta CFS$ results

245 for a given depth (Fig. 3). Larger friction coefficients tend to increase the $\Delta CFS$ amplitude and

246 changes the spatial distribution of positive and negative stress changes (Fig. 3). This is similar to

247 Barnhart et al. (2019), where they found that their results are consistent for all friction coefficients

248 that they tested. For a given friction coefficient, changing the depth of the $\Delta CFS$ calculation from

249 5 km to 10 km increases the $\Delta CFS$ amplitude by ~0.3 MPa and decreases the extent of the region

250 of positive $\Delta CFS$ on the Garlock fault by approximately 20 km (Fig. 3). The amplitude difference

251 is because the largest portion of mainshock slip extends to about 10 km depth, and the change in

252 slip at this depth produces a larger $\Delta CFS$ than at 5 km depth. The region of positive $\Delta CFS$ in

253 proximity to the creeping section of the Garlock fault is most consistent in spatial extent with that

254 of Barnhart et al. (2019) when we use a friction coefficient of 0.2 and a depth of 5 km. Lastly, we

255 find that the cluster of aftershocks on the Garlock fault are unlikely to be simply explained by

256 $\Delta CFS$ from the mainshock as the value of the stress change can be small (< 0.01 MPa) or even

257 negative (~ -0.1 MPa) [Fig. 3].

258 *Dynamic Earthquake Rupture model*

259        Our first goal is to explain the kinematic fault slip distribution using rupture dynamics. We

260 seek to reproduce the two primary patches of 2.5 m and 4.7 m slip southeast and northwest of the

261    hypocenter, respectively, (Fig. 1b; 5a). We show the rupture history until 35 seconds to highlight
262    the arrest of both the northwest and southeast rupture fronts (Fig. 5).

263         The initial conditions and friction parameters outlined in the methods section gives a good
264    agreement between the kinematically imaged and dynamically modeled slip distributions. The
265    exception is the region near the hypocenter, where the dynamic rupture model overpredicts the
266    kinematic slip amplitude by ~0.8 meters (Fig. 5a). This is most likely due to our time-weakening
267    nucleation procedure, but is probably within the uncertainty of the true fault slip resolved by the
268    kinematic inversion. The distribution in dynamic stress drop is positive where higher slip is
269    concentrated, and negative in a small region southeast of the hypocenter and where we impose
270    slip-strengthening frictional behavior at the ends of the fault (Fig. 5b).

271         The bilateral mainshock dynamic rupture is overall heterogeneous and spatiotemporally
272    complex (Fig. 5c). There are three major asperities (i.e., relatively high dynamic stress-drop
273    regions) that contribute to several rupture-front accelerations (Fig. 5b, c). The model shows a slow
274    (< 1 km/s) rupture front propagating to the southeast for the first five seconds after nucleation
275    ceases; this southeast rupture front then accelerates to ~1.3 km/s before decelerating and arresting
276    at 28 seconds (Fig. 5c). In contrast, the northwest rupture front propagates at a more uniform speed
277    (~2.1 km/s) before decelerating and stopping at ~25 seconds. These rupture speeds are consistent
278    with recent kinematic models that prescribe a constant sub-Rayleigh mainshock rupture speed
279    (Goldberg et al., 2020; Liu et al., 2019; Ross et al., 2019; Zhang et al., 2020). Rupture speed
280    depends on how much total available energy is partitioned into radiated or fracture energy during
281    the faulting process. Slower ruptures (as observed during the Ridgecrest sequence) may be due to
282    a relatively high fracture energy consumed on the fault, consistent with the hypothesis that the Llfz
283    is less compliant and more energy was needed to break multiple fault segments (Goldberg et al.,
284    2020; Liu et al., 2019; Perrin et al., 2016). Our dynamic model shows that the mainshock rupture
285    fronts do not exhibit slip-rate amplitudes above 4 m/s and propagate at well below the Rayleigh
286    wave speed.

287    *Temporal Stress Changes on the Garlock fault*

288         Using our dynamic rupture model, we investigate the stress contributions to a section of
289    the central Garlock fault during and after the Ridgecrest mainshock. Note that given the
290    limitation of our modeling domain, we cannot assess far-field dynamic stress contributions from

291  surface-wave amplitude changes. We instead focus on how the initial peak stresses carried by

292  near-field seismic waves impacted the Garlock fault during coseismic rupture.

293      The 2-D stress tensor in our model is for an isotropic body and yields three unique

294  components: $\sigma_{xx}$, $\sigma_{yy}$, and $\sigma_{xy}$. Only one component of the normal stress ($\sigma_{yy}$) and the shear stress

295  ($\sigma_{xy}$) are important to be considered further in our analysis. If we place the strike of the mainshock

296  fault plane on an east-west coordinate system, the angle between the mainshock and Garlock fault

297  planes (measured clockwise) is approximately 110 degrees. We therefore applied a rotation of the

298  stress field at a particular instant in time to represent the stress perturbation the mainshock imparts

299  to the Garlock fault (Fig. 6 see Supplemental Information). When this rotation is performed at the

300  final time-step, the rotated stress field is equivalent to the static stress change on the Garlock fault.

301  We observe an abrupt transition from negative to positive normal static stress change as one

302  crosses the intersection of the strike of the mainshock fault plane (Fig. 7a). The shear stress change

303  is slightly more complex with an asymmetric stress amplitude distribution across the fault, but

304  shows a very pronounced region of positive stress change that generally coincides with the ~25-

305  km long section of the central Garlock fault that underwent creep (Fig. 7b; Barnhart et al., 2019;

306  Xu et al., 2019). To confirm our static stress change analysis from the dynamic model, we compare

307  it to our $\Delta CFS$ calculation and find that its orientation and amplitude are consistent (Fig. S4).

308      We also calculate the temporal stress change on the central Garlock fault segment during

309  the Ridgecrest mainshock. We select one point near the creeping region on the Garlock fault (-60

310  km, -10 km; Fig. 7 and  8) to show how normal and shear stresses change during mainshock

311  rupture. While propagation spontaneously arrests at near ~28 seconds towards the southeast, we

312  simulate rupture until 100 seconds to make sure stress changes relax to constant levels, which are

313  attained at 60 seconds (Fig. 9). This section of the central Garlock fault begins to experience a

314  positive normal stress change near 17.5 seconds (Fig. 7). During the main portion of coseismic

315  rupture, normal stress changes reach their maximum of ~0.3 MPa at 32 seconds (Fig. 7f, 9a). In

316  contrast, positive shear stress changes arrive at the Garlock fault in three distinct pulses (e.g., Fig.

317  8f, 9a). Two of these positive shear stress change pulses arrive after the largest change in normal

318  stress change and continue to be above the normal stress change amplitude for the remainder of

319  our simulation (Fig. 8, 9a). The extrema of the normal and shear stress change amplitudes are

320  symmetric through time due to the alternating arrivals of compressional (P) and shear (SV) wave

321  motions.

322 **Discussion and Conclusion**

323     We show that stress changes during and after the Ridgecrest foreshocks and mainshock
324 may have influenced post-seismic creep on the central Garlock fault segment and brought certain
325 regions potentially closer to coseismic failure. Our results also shed light on the temporal stress
326 evolution on the Garlock fault due to source dynamics. Because both normal and shear stresses
327 vary during coseismic rupture, evaluating their respective contribution is of critical importance to
328 identifying periods when stresses changes may have been favorable to engender the observed post-
329 seismic creep.

330     The Coulomb stress change results show that positive static stress changes were
331 experienced on the central Garlock fault due to mainshock slip (Fig. 3) and are coincident with
332 previously documented fault creep (Barnhart et al., 2019; Ross et al., 2019; Xu et al., 2020).
333 Among Coulomb stress changes calculated for different friction levels and depths, in only one case
334 (i.e., friction level of 0.6) is a positive static stress change on the order of ~0.1 MPa observed
335 adjacent to the region of the Garlock fault that experienced a sizeable aftershock swarm (Fig. 3).
336 This may indicate that other post-seismic relaxation processes or dynamic stress changes were at
337 play to produce this aftershock pattern. Various studies have also calculated the Coulomb stress
338 change of the foreshock at the mainshock hypocenter with their slip inversion results. While
339 Barnhart et al (2019) found an increase in Coulomb stress change of 0.6 MPa due to the foreshock
340 at their hypocenter, Zhang et al. (2020) found an increase of 0.04 MPa and Goldberg et al. (2020)
341 found a <0.1 MPa increase. we find that a 0.1 MPa decrease in Coulomb stress change at the
342 location of our hypocenter. The disparity in magnitude and sign of the results may be due to the
343 fact that Coulomb stress calculations are very sensitive to the slip inversion model used and the
344 inferences may change depending on the location of the hypocenter, as well.

345     When we assess the $\Delta CFS$ through time we find that $\Delta CFS$ predominantly increases during
346 mainshock rupture and remains at a high level afterwards; this is evident from our dynamic model
347 as the normal stress change amplitude is mostly below the shear stress amplitude (Fig. 9b).
348 Temporal stress changes during the mainshock rupture also support predominantly positive shear
349 stress changes near this creeping Garlock region (Fig. 8), whereas positive and negative normal
350 stress distributions are observed on both sides of the projected intersection of the mainshock and
351 Garlock fault planes (Fig. 7). Our results for temporal normal and shear stress changes near the
352 Garlock fault agree with other dynamic rupture simulations that prescribe a complex 3-D fault

11

353   geometry, but similar constitutive friction law parameters (Lozos and Harris, 2020). Moreover,
354   this study also documents a detailed temporal evolution of normal, shear, and Coulomb stresses
355   impacting the central Garlock fault (i.e., Fig. 9), and not just the final stress changes after all
356   seismic waves have been radiated away. Because positive normal stress changes serve to
357   strengthen the fault whereas positive shear stresses should bring the fault closer to failure, our
358   dynamic model offers one possible scenario that creep could have occurred as soon as ~15 seconds
359   after nucleation of the Ridgecrest mainshock when positive shear stresses began to arrive at the
360   Garlock fault. However, this is speculative given that we do not have information on the absolute
361   stress state of the Garlock fault prior to the aftershock/mainshock sequence.

362        Our dynamic model also suggests that the largest shear stress changes (0.3 – 0.4 MPa)
363   arrived before and after the largest normal stress changes, but they are comparable in amplitude
364   (Fig. 7, 8, 9a). Given this maximum shear stress change amplitude at a given time, we estimate
365   approximately 0.1 centimeters of slip may have been triggered near the creeping section of the
366   Garlock fault at a depth less than 1 km (Fig. S5a). We also test a model where creep on the Garlock
367   fault was exceptionally shallow (< 300 m depth; Schleicher et al., 2019) but the distribution of
368   creep is more heterogeneous. We still obtain a similar amount of creep that is consistent with the
369   shear stress change amplitude (Fig. S5b). These estimates are lower than the maximum magnitude
370   of resolved surface creep (i.e., ~3 cm) documented earlier by Barnhart et al., (2019) and Ross et
371   al., (2019), however. The creep magnitudes we estimate are furthermore only valid for a
372   homogenous, Poisson solid and should be considered an upper-bound for any given shear stress-
373   change perturbation because our dynamic rupture model captures the region on the mainshock
374   fault plane that experiences the greatest dynamic stress-drop (~7 MPa; Fig. 5b). There is potential
375   for more creep to be accommodated by successive near-field stress changes arriving at the Garlock
376   fault during mainshock rupture, but this depends on the near-surface rheology and earthquake
377   history of the central Garlock fault. Additionally, we cannot rule out the possibility that the
378   maximum resolvable creep was driven by cumulative or post-seismic strain-rate changes not seen
379   by satellite observations since the smallest observation window is at least five to six days after the
380   mainshock (Barnhart et al., 2019). But extensometer data imply that it did not extend very deep
381   into the crust, regardless of how much triggered creep was (Bilham and Castillo, 2020).

382        The fact that the Garlock fault did not coseismically fail could be supported by theoretical
383   considerations to the prestress state, rupture speed and fault orientation between the mainshock

384  and Garlock fault planes if they are connected (Poliakov et al., 2002; Kame et al., 2003). For a low

385  angle of maximum horizontal shear stress (SH_max) with respect to the fault (< 45 degrees), this

386  prestress state encourages rupture to bifurcate towards the compressional side, whereas a higher

387  angle (> 45 degrees) predicts that the rupture along the extensional side is more favorable

388  (Poliakov et al., 2002). Yang and Hauksson (2013) inverted earthquake focal mechanisms in

389  central and southern California, estimating the regional SH_max orientation lies between zero and

390  five degrees east of North. Our dynamic rupture model predicts an average mainshock rupture-

391  front to shear-wave speed ratio of 0.4. Given that the mainshock fault plane is approximately

392  oriented 45 degrees west of North, such a low prestress orientation together with low rupture speed

393  levels are not likely to encourage rupture propagation to the Garlock fault, if connected (Kame et

394  al., 2003). This mechanical argument, however, must be taken with a grain of salt considering

395  changes in the local stress field orientation surrounding the M7.1 mainshock due to the M6.4,

396  smaller foreshocks, and other seismicity. A detailed seismological analysis of foreshock and

397  aftershock stress-tensor inversions will undoubtedly place stronger constraints on the SH_max

398  orientation to the mainshock fault plane, and perhaps lend credence to theoretical expectations we

399  have briefly discussed here.

400      One aspect we could continue to explore in greater detail is how a fully dynamic model

401  incorporating segmented foreshock and mainshock fault planes changes the details of the temporal

402  stress changes on the Garlock fault. Several kinematic studies are able to fit seismogeodetic data

403  using a segmented fault model (e.g., Goldberg et al., 2020; Liu et al., 2019; Ross et al., 2019).

404  Given that the Ridgecrest sequence produced multiple orthogonal faulting with some ruptures

405  breaking the surface while others not (Ross et al., 2019), we would expect the temporal stress

406  change to accordingly reflect this complexity. We note that the geometrically segmented 3-D

407  dynamic fault model by Lozos and Harris (2020) yields static normal and shear stress changes on

408  the Garlock fault that are consistent to first-order in sign and amplitude with our modelling efforts.

409  There are small differences, but this is expected due to different initial stress parameterizations,

410  velocity structure, and fault geometry for the mainshock and foreshock fault planes.

411      How the M6.4 foreshock and M7.1 mainshock Ridgecrest sequences changed the local

412  stress field in Southern California is a crucial question to consider given the proximity of these

413  events to other active faults (e.g., Garlock and San Andreas). Through a unique combination of

414  kinematic, static, and dynamic modeling, we present a physically coherent picture of the stress

415  changes on the central Garlock fault during and after the coseismic rupture of the M7.1 event. We

416  find that positive stress changes near the creeping section of the Garlock fault are observed during

417  and after coseismic rupture. We also show that the greatest shear stress change was comparable to

418  the greatest normal stress change, but arrived earlier during dynamic rupture; this may have

419  promoted a section of the Garlock fault to creep even before the Ridgecrest mainshock finished

420  slipping. Our dynamic models physically explain the resolved slip amplitude through the

421  mainshock hypocenter and reproduce the low sub-Rayleigh rupture speeds previously suggested

422  by kinematic rupture models.

423  **Data and Resources**

424  Static stress calculations are conducted using the Coulomb 3 software available from the

425  USGS website, https://earthquake.usgs.gov/research/software/coulomb/. All codes used in

426  dynamic model post-processing and figure creation as well as model input and output files are

427  archived and freely accessible on UM Deep Blue (https:// deepblue.lib.umich.edu/). Data used in

428  the kinematic inversion are available upon request to Dr. Shengji Wei (shjwei@ntu.edu.sg). Some

429  figures in this paper were generated with MATLAB™ software or used colormap schemes from

430  Crameri (2018, http://doi.org/10.5281/zenodo.1243862).

431

439

440

441

442

443

444

445

**References**

Allen, C. R., Wyss, M., Brune, J. N., Grantz, A., and Wallace, R. E. (1972). Displacements on the Imperial, Superstition Hills, and San Andreas faults triggered by the Borrego Mountain earthquake, in The Borrego Mountain Earthquake of April 9, 1968. *U.S. Geol. Sur. Profess. Paper,* 787, 87-104.

Ampuero, J. P. (2009). SEM2DPACK: A spectral element method tool for 2D wave propagation and earthquake source dynamics, User's Guide, version 2.3.6. Retrieved from http://www.sourceforge.net/projects/sem2d/

Andrews, D. J. (1985). Dynamic plane-strain shear rupture with a slip-weakening friction law calculated by a boundary integral method. *Bull. Seismo. Soc. Of Amer.*, 75(1), 1–21.

Astiz, Luciana, Allen, C. R. (1983). Seismicity of the Garlock fault, California. *Bull. of the Seismo. Soc. of Amer.*, 73(6), 1721–1734. https://doi.org/10.1017/CBO9781107415324.004

Barnhart, W. D., Hayes, G. P., & Gold, R. D. (2019). The July 2019 Ridgecrest, California, Earthquake Sequence: Kinematics of Slip and Stressing in Cross-Fault Ruptures. *Geophys. Res. Lett.*, (July), 859–867. https://doi.org/10.1029/2019GL084741

Bilham, R., and B. Castillo (2020). The July 2019 Ridgecrest, California, Earthquake Sequence Recorded by Creepmeters: Negligible Epicentral Afterslip and Prolonged Triggered Slip at Teleseismic Distances, *Seismol. Res. Lett.* XX, 1–14, doi: 10.1785/0220190293.

Bodin, P. and Gomberg, J. (1994). Triggered Seismicity and Deformation between the Landers, California, and Little Skull Mountain, Nevada, Earthquakes. *Bulletin of the Seismological Society of America*, 84, 3, 835-843.

Brodsky, E. E., Mori, J. J., Anderson, L., Chester, F. M., Conin, M., Dunham, E. M., … Yang, T. (2020). The State of Stress on the Fault Before, During, and After a Major Earthquake. *Annu. Rev. Earth Planet. Sci*, 48(1), annurev-earth-053018-060507. https://doi.org/10.1146/annurev-earth-053018-060507

Dawson, T. E., McGill, S. F., & Rockwell, T. K. (2003). Irregular recurrence of paleoearthquakes along the central Garlock fault near El Paso Peaks, California. *Jour. of Geophys. Res: Solid Earth*, 108(B7). https://doi.org/10.1029/2001jb001744

Goldberg, D. E., Melgar, D., Sahakian, V. J., Thomas, A. M., Xu, X., Crowell, B. W., & Geng, J. (2020). Complex Rupture of an Immature Fault Zone: A Simultaneous Kinematic Model of the 2019 Ridgecrest, CA Earthquakes. *Geophysical Research Letters*, 47(3), 1–10. https://doi.org/10.1029/2019GL086382

Hill, M. L. and T W. Dibblee (1953). San Andreas, Garlock and Big Pine faults, California, Bull. *Geol Soc Am*, 64, 443-458.

489  Ji, C., D.J. Wald, and D.V. Helmberger (2002). Source description of the 1999 Hector Mine,
490       California earthquake; Part I: Wavelet domain inversion theory and resolution analysis,
491       *Bull. Seism. Soc. Am.*, Vol 92, No. 4. pp. 1192-1207.

493  Kame, N., Rice, J. R., & Dmowska, R. (2003). Effects of prestress state and rupture velocity on
494       dynamic fault branching. *Jour. of Geophys. Res: Solid Earth*, 108(B5), 1–21.
495       https://doi.org/10.1029/2002jb002189

497  Kendrick, K. J. et al., Southern California Earthquake Center Annual Meeting Proceedings (SCEC,
498       2019), contribution 9779.

500  King, G. and J. Nabelek, (1985). The role of fault bends in the initiation and termination of
501       earthquake rupture. *Science*, 228, 984-987.

503  Lienkaemper, J. J., Galehouse, J. S., Simpson, R. W. (1997). Creep response of the Hayward fault
504       to stress changes caused by the Loma Prieta earthquake. *Science,* 276, 5321, 2014-2016.
505       DOI: 10.1126/science.276.5321.2014

507  Lin, J. and R.S. Stein (2004). Stress triggering in thrust and subduction earthquakes, and stress
508       interaction between the southern San Andreas and nearby thrust and strike-slip faults. *J. of*
509       *Geophys. Res.,* 109, B02303, doi:10.1029/2003JB002607.

511  Liu, C., Lay, T., Brodsky, E. E., Dascher-Cousineau, K., & Xiong, X. (2019). Coseismic Rupture
512       Process of the Large 2019 Ridgecrest Earthquakes From Joint Inversion of Geodetic and
513       Seismological Observations. *Geophys. Res. Lett*. https://doi.org/10.1029/2019GL084949

514  Lozos, J. C., & Harris, R. A. (2020). Dynamic Rupture Simulations of the M6 . 4 and M7 . 1 July
515       , 2019 Ridgecrest , California Earthquakes. *Geophysical Research Letters*, 1–16.
516       https://doi.org/10.1029/2019GL086020

517  Ma, S. and Archuleta, R.J., (2006). Radiated seismic energy based on dynamic rupture models of
518       faulting, *J. Geophys. Res.*, 111, doi:10.1029/2005JB004055.

520  Madugo, C. M., Dolan, J. F., & Hartleb, R. D. (2012). New paleoearthquake ages from the western
521       Garlock fault: Implications for regional earthquake occurrence in Southern California. *Bull.*
522       *of the Seismo. Soc. of Amer.*, 102(6), 2282–2299. https://doi.org/10.1785/0120110310

524  McGill, S. F., and K. Sieh (1991). Surficial offsets on the central and eastern Garlock fault
525       associated with prehistoric earthquakes, *J. Geophys. Res.*, 96, 21,597–21,621.

527  Noda, H., and N. Lapusta (2013). Stable creeping fault segments can become destructive as a result
528       of dynamic weakening, *Nature*, 493, 518–521, doi:10.1038/nature11703.

530  Perrin, C., Manighetti, I., Ampuero, J.-P., Cappa, F., & Gaudemer, Y. (2016). Location of largest
531       earthquake slip and fast rupture controlled by along-strike change in fault structural maturity

532    due to fault growth. *Jour. of Geophys. Res: Solid Earth*, 121(5), 3666–3685.
533    https://doi.org/10.1002/2015JB012671

535    Poliakov, A. N. B., Dmowska, R., & Rice, J. R. (2002). Dynamic shear rupture interactions with
536    fault bends and off-axis secondary faulting. *Jour. of Geophys. Res.*, 107(B11), ESE 6-1-
537    ESE 6-18. https://doi.org/10.1029/2001jb000572

539    Rice, J. R. (1992). Fault Stress States, Pore Pressure Distributions, and the Weakness of the San
540    Andreas Fault. *Inter. Geophys.*, 51(C), 475–503. https://doi.org/10.1016/S0074-
541    6142(08)62835-1

543    Ripperger, J., & Mai, P. M. (2004). Fast computation of static stress changes on 2D faults from
544    final slip distributions. *Geophy. Res. Lett.*, 31(18), 2–5.
545    https://doi.org/10.1029/2004GL020594

547    Ross, Z. E., Idini, B., Jia, Z., Stephenson, O. L., Zhong, M., Wang, X., … Moore, A. W. (2019).
548    2019 Ridgecrest earthquake sequence. Science, 3665(October), 346–351.

550    Schleicher, L. S., Huang, M., Allison, K. L., and Anderson, R. J. (2019). Seismic hazard
551    implications of post-seismic deformation and stress transfer from the 2019 Searles Valley
552    California Earthquakes, Abstract S41C-08 presented at 2019 Fall Meeting, AGU, San
553    Francisco, CA, 9-14 Dec., 2019.

555    Toda, S., R. S. Stein, K. Richards-Dinger and S. Bozkurt (2005). Forecasting the evolution of
556    seismicity in southern California: Animations built on earthquake stress transfer. *J.
557    Geophys. Res.*, 110, B05S16, doi:10.1029/2004JB003415.

559    Tinti, E., Cocco, M., Fukuyama, E., & Piatanesi, A. (2009). Dependence of slip weakening
560    distance (Dc) on final slip during dynamic rupture of earthquakes. *Geophys. Jour. Int.*,
561    177(3), 1205–1220. https://doi.org/10.1111/j.1365-246X.2009.04143.x

563    Xu, X., D. T. Sandwell, and B. Smith-Konter (2020). Coseismic Displacements and Surface
564    Fractures from Sentinel-1 InSAR: 2019 Ridgecrest Earthquakes, Seismol. Res. Lett. XX,1–
565    7, doi: 10.1785/ 0220190275.

567    Yang, W. and Hauksson, E., (2013). The tectonic crustal stress field and style of faulting along the
568    Pacific North America Plate boundary in Southern California, *Geophys. Jour. Int.*, 194, 100-
569    117, doi: 10.1093/gji/ggt113

571    Zhang, Y., X. Zheng, Q. Chen, X. Liu, X. Huang, Y. Yang, Q. Xu, and J. Zhao (2020). Automatic
572    Inversion of Rupture Processes of the Foreshock and Mainshock and Correlation of the
573    Seismicity during the 2019 Ridgecrest Earthquake Sequence, Seismol. Res. Lett. XX, 1–11,
574    doi: 10.1785/0220190343.

17

578   **Author Mailing Addresses**
579       1.  Marlon D. Ramos, Jing Ci Neo, Prithvi Thakur, Yihe Huang
580       2.  Shengji Wei
581
582   Authors one through four may be contacted at:
583
584                   Department of Earth and Environmental Sciences
585                               University of Michigan
586                                   Room 2534
587       Attn: Marlon D. Ramos, Jing Ci Neo, Prithvi Thakur, Yihe Huang
588                           1100 North University Avenue
589                             Ann Arbor, MI 48109-1005
590   Author five may be contacted at:
591                           Earth Observatory of Singapore
592                         Nanyang Technological University
593                               Attn: Wei Shengji
594                                  N2-01A-08
595                     50 Nanyang Ave, Singapore 639798
596
597
598
599
600
601   **List of Tables**
602
603
604                                     **Table 1**
605   Coulomb stress-change parameters of the mainshock and aftershock fault planes. Hypocenter
606   location (latitude, longitude, depth) and maximum slip amplitude (meters) from the kinematic
607   inversion are also listed.
608

|  | $M_w$ | Hypocenter | Strike | Dip | Rake | Peak Slip (m) |
|---|---|---|---|---|---|---|
| **Mainshock** | 7.1 | 35.772N -117.602E 3 km | 322 | 81 | -170 | 4.7 |
| **Foreshock** | 6.4 | 35.705N -117.506E 9 km | 318 | 88 | -172 | 1.3 |
|  |  |  | 228 | 81 | 0 | 0.74 |

609
610
611
612
613
614
615
616
617

618 **List of Figure Captions**
619
620 **Figure 1.** 2019 Ridgecrest Earthquake Sequence. (a) Study area with foreshock and mainshock
621 fault planes denoted by solid lines. The approximate region of the central Garlock fault that
622 experienced creep during this sequence is indicated by the box. (b) Mainshock slip-inversion
623 results where we determine a hypocenter depth of 3 km and a peak slip amplitude of 4.7 m that is
624 immediately northwest of the hypocenter. (c) Foreshock slip-inversion results. Foreshock planes
625 parallel and perpendicular to the mainshock fault plane are denoted as Plane 1 and Plane 2,
626 respectively. Note that the northwest-southeast fault orientation is the same for the mainshock and
627 foreshock fault planes. Stars indicate epicenter (figure a) or hypocenter (figures b and c) locations.
628 The color version of this figure is available only in the electronic edition.
629
630 **Figure 2.** Coulomb stress-change due to foreshock Planes 1 and 2 on the mainshock fault plane
631 calculated at a depth of 5 km and with a friction coefficient of 0.6. (a) The combined effect of both
632 aftershock fault plane slip on the mainshock. (b) The Coulomb stress change from Plane 1 which
633 is parallel to the main fault plane. (c) Coulomb stress change from Plane 2,which is the NE-SW
634 striking cross-fault. The aftershocks depicted are the earthquakes that occurred after the foreshock
635 and do not include those induced from mainshock stress changes. The color version of this figure
636 is available only in the electronic edition.
637
638 **Figure 3**. Coulomb stress change of the mainshock on a receiver fault of 70° strike and 90° dip,
639 approximating the leftmost part of the Garlock fault in this figure. Top: Coulomb stress-change
640 results for a 5 km depth source at friction coefficients of (left to right) 0.2, 0.4, and 0.6. Bottom:
641 Coulomb stress-change results for a 10 km depth source with the same friction coefficients. The
642 color version of this figure is available only in the electronic edition.
643
644 **Figure 4**. Static stress-drop (top) and initial shear stress (bottom) along the mainshock fault
645 plane. Static stress-drop is calculated assuming a homogeneous, Poisson medium and initial
646 shear stress is computed using the complete stress-drop assumption. We select an initial shear
647 stress profile through the main asperity at 3 km depth (dashed line) as a starting condition for our
648 2-D dynamic rupture models.
649
650 **Figure 5**. (a) Along-fault slip distribution resolved by the kinematic slip inversion (solid line) and
651 that calculated from the dynamic rupture model (dashed line). The x-axis measures distance from
652 where the earthquake is nucleated in our model. (b) Dynamic stress-drop along the fault. Location
653 shown in Figure 4. (c) Spatiotemporal and bilateral rupture history predicted by the dynamic
654 rupture model. Colorbar denotes slip-rate and the slope of the gradient between zero and peak slip-
655 rate signifies and average rupture front speed (solid lines). Both rupture fronts propagate at sub-
656 Rayleigh wave speed.
657
658 **Figure 6**. Static stress-change field in the modeling domain rotated to the strike of the Garlock
659 fault. (a) normal stress and (b) shear stress. Garlock fault trace (dashed line) and Ridgecrest
660 mainshock fault (solid line) are superimposed onto the figure. Box denotes approximate location
661 of the creeping region (Barnhart et al., 2019). Spatial orientation is the same for figures 6 – 8. The
662 color version of this figure is available only in the electronic edition.
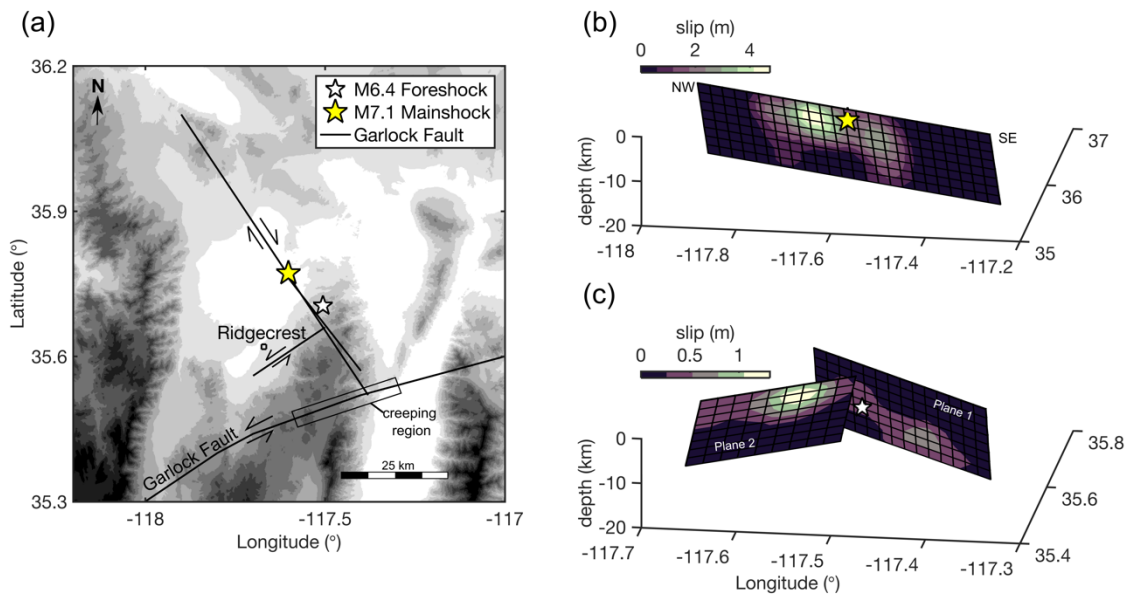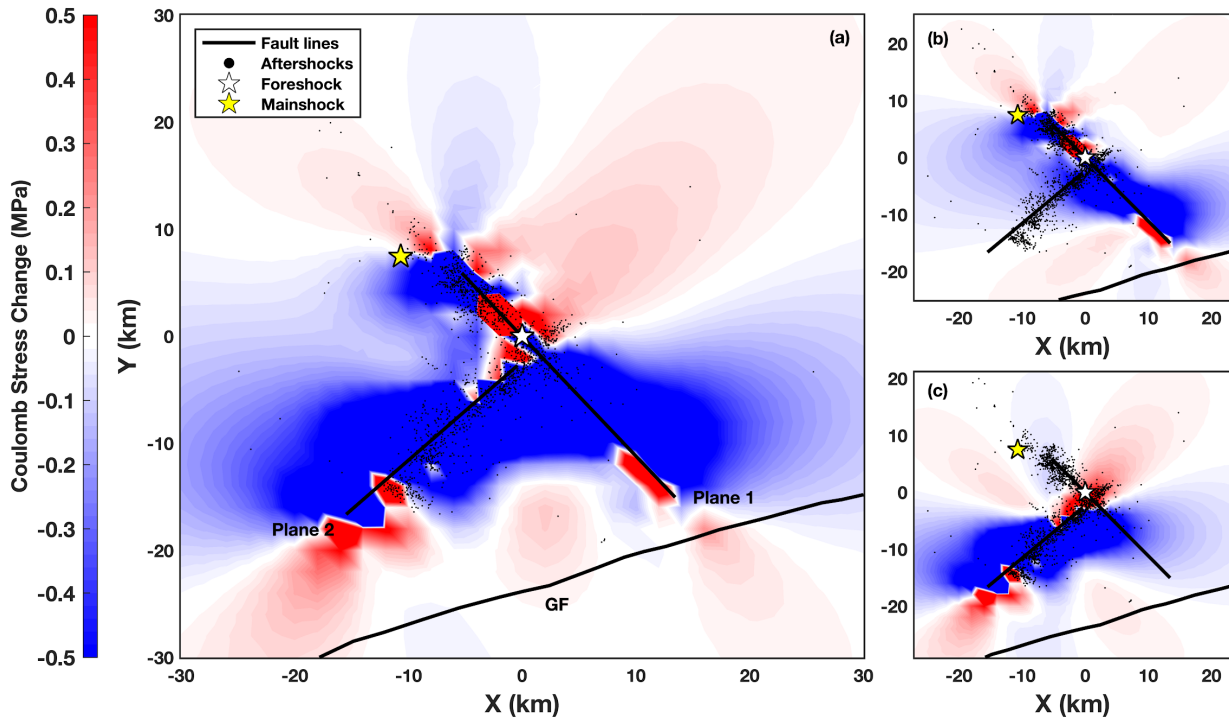
663

664     **Figure 7**. Normal stress changes ($\sigma$ $yy$) at various moments in time on the central Garlock fault
665     during coseismic rupture of the mainshock. A point on the Garlock is selected to visualize the
666     stress amplitude variability (solid circle). Subfigures (a) through (e) represent $\sigma$ $yy$ from 17.5 to
667     50 seconds during rupture propagation. (f) shows the time-history of $\sigma$ $yy$ where the blue squares
668     denote the amplitude change at each of the normal stress snapshots (a-e).

669

670     **Figure 8**. Similar to Fig. 9, but shear stress changes ($\sigma_{xy}$) during coseismic rupture. $\sigma_{xy}$ exhibits
671     three distinct peaks in its temporal stress-change on the Garlock fault at ~28, 38, and 50 seconds.

672

673     **Figure 9.** Stress change evolution on a section of the Garlock fault during the entire Ridgecrest
674     earthquake simulation. (a) Normal ($\sigma$ $yy$) and shear ($\sigma$ $xy$) stress change. (b) Temporal
675     Coulomb stress change for friction coefficient levels assessed in the static stress change analysis.
676     Note that we plot the temporal stress change starting at 10 seconds because this is when the
677     nucleation procedure ceases.

678

679
680
681
682
683
684
685
686
687
688
689
690
691
692
693
694
695
696
697
698
699
700
701
702
703
704
705
706
707

708 **Figures**
709
710



711
712 **Figure 1.** 2019 Ridgecrest Earthquake Sequence. (a) Study area with foreshock and mainshock
713 fault planes denoted by solid lines. The approximate region of the central Garlock fault that
714 experienced creep during this sequence is indicated by the box. (b) Mainshock slip-inversion
715 results where we determine a hypocenter depth of 3 km and a peak slip amplitude of 4.7 m that is
716 immediately northwest of the hypocenter. (c) Foreshock slip-inversion results. Foreshock planes
717 parallel and perpendicular to the mainshock fault plane are denoted as Plane 1 and Plane 2,
718 respectively. Note that a northwest-southeast fault orientation is the same for the mainshock and
719 foreshock fault planes. Stars indicate epicenter (a) or hypocenter (b and c) locations. The color
720 version of this figure is available only in the electronic edition.
721
722
723
724

725



726
727 **Figure 2.** Coulomb stress-change due to foreshock Planes 1 and 2 on the mainshock fault plane
728 calculated at a depth of 5 km and with a friction coefficient of 0.6. (a) The combined effect of both
729 aftershock fault plane slip on the mainshock. (b) The Coulomb stress change from Plane 1 which
730 is parallel to the main fault plane. (c) Coulomb stress change from Plane 2, which is the NE-SW
731 striking cross-fault. The aftershocks depicted are the earthquakes that occurred after the foreshock
732 and do not include those induced from mainshock stress changes. The color version of this figure
733 is available only in the electronic edition.
734
735
736

737



738
739 **Figure 3.** Coulomb stress change of the mainshock on a receiver fault of 70° strike and 90° dip,
740 approximating the leftmost part of the Garlock fault in this figure. Top: Coulomb stress-change
741 results for a 5 km depth source at friction coefficients of (left to right) 0.2, 0.4, and 0.6. Bottom:
742 Coulomb stress-change results for a 10 km depth source with the same friction coefficients. The
743 color version of this figure is available only in the electronic edition.
744
745
746
747
748
749
750
751
752
753
754
755
756
757
758
759
760
761

762
763
764



765
**Figure 4.** Static stress-drop (top) and initial shear stress (bottom) along the mainshock fault plane. Static stress-drop is calculated assuming a homogeneous, Poisson medium and initial shear stress is computed using the complete stress-drop assumption. We select an initial shear stress profile through the main asperity at 3 km depth (dashed line) for our 2-D dynamic rupture models.

770

771
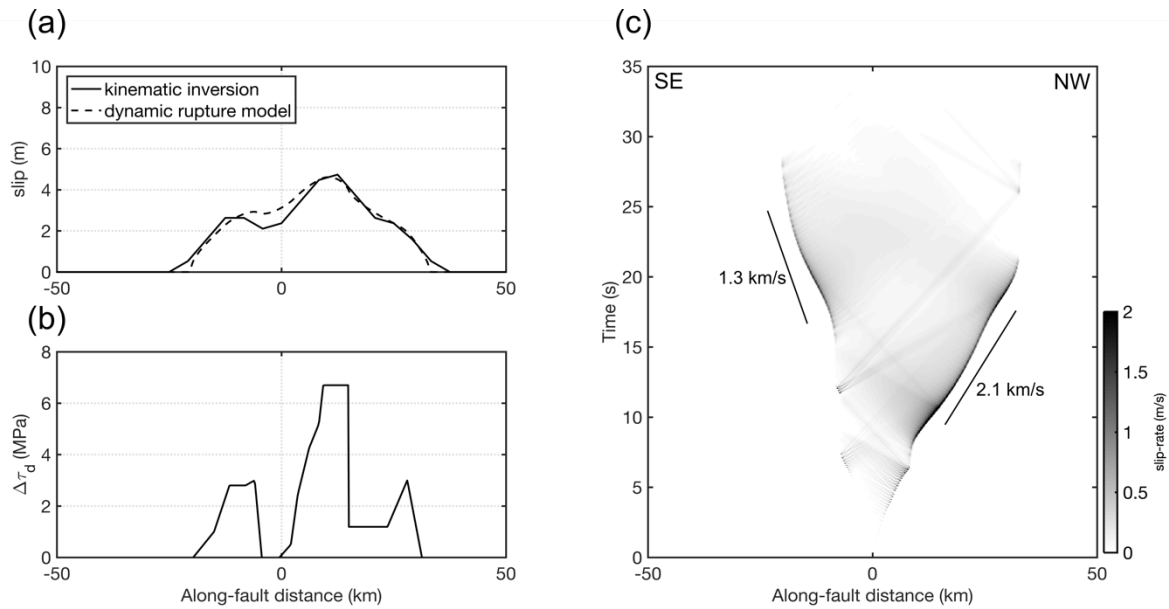
772



774 **Figure 5.** (a) Along-fault slip distribution resolved by the kinematic slip inversion (solid line) and
775 that calculated from the dynamic rupture model (dashed line). The x-axis measures distance from
776 where the earthquake is nucleated in our model. (b) Dynamic stress-drop along the fault. Location
777 shown in fig 4. (c) Spatiotemporal and bilateral rupture history predicted by the dynamic rupture
778 model. Colorbar denotes slip-rate and the slope of the gradient between zero and peak slip-rate
779 signifies average rupture front speed (solid lines). Both rupture fronts propagate at sub-Rayleigh
780 wave speed.

781
782
783
784
785
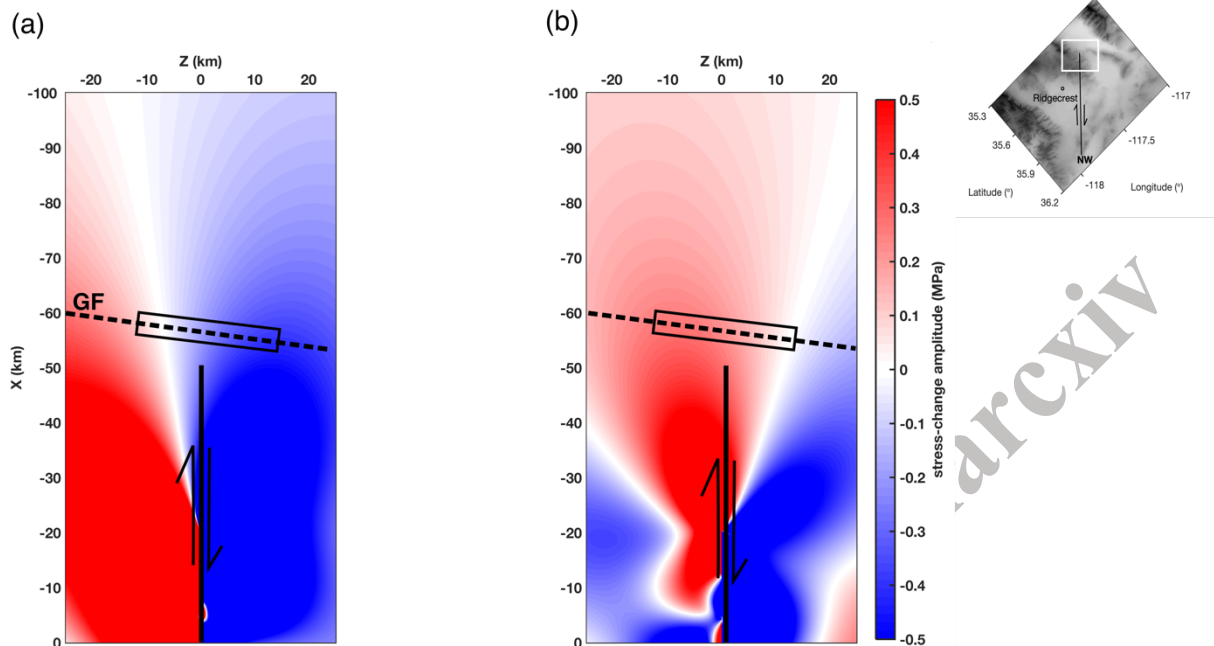
786
787 **Figure 6.** Static stress-change field in the modeling domain rotated to the strike of the Garlock
788 fault. (a) normal stress and (b) shear stress. Garlock fault trace (dashed line) and Ridgecrest
789 mainshock fault (solid line) are superimposed onto the figure.  Box denotes approximate location
790 of the creeping region (Barnhart et al., 2019). Spatial orientation is the same for figures 6 – 8. The
791 color version of this figure is available only in the electronic edition.
792
793
794
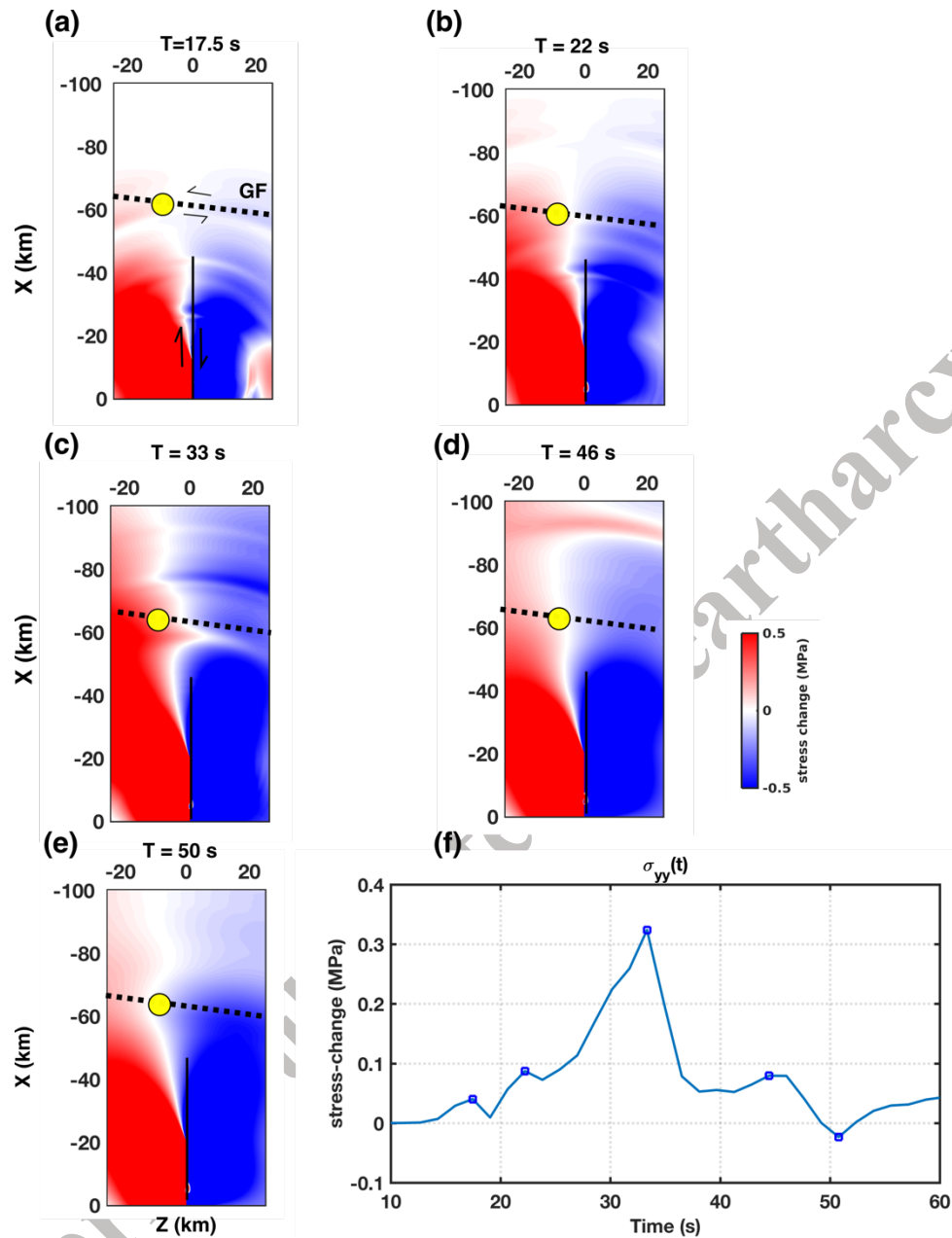795
796
797
798
799
800
801
802
803
804
805
806
807
808
809
810
811
812
813
814

815
816 **Figure 7.** Normal stress changes ($\sigma_{yy}$) at various moments in time on the central Garlock fault
817 during coseismic rupture of the mainshock. A point on the Garlock is selected to visualize the
818 stress amplitude variability (solid circle). Subfigures (a) through (e) represent $\sigma_{yy}$ from 17.5 to 50
819 seconds during rupture propagation. (f)shows the time-history of $\sigma_{yy}$ where the blue squares
820 denote the amplitude change at each of the normal stress snapshots (a-e). The color version of this
821 figure is available only in the electronic edition.
822
823
824
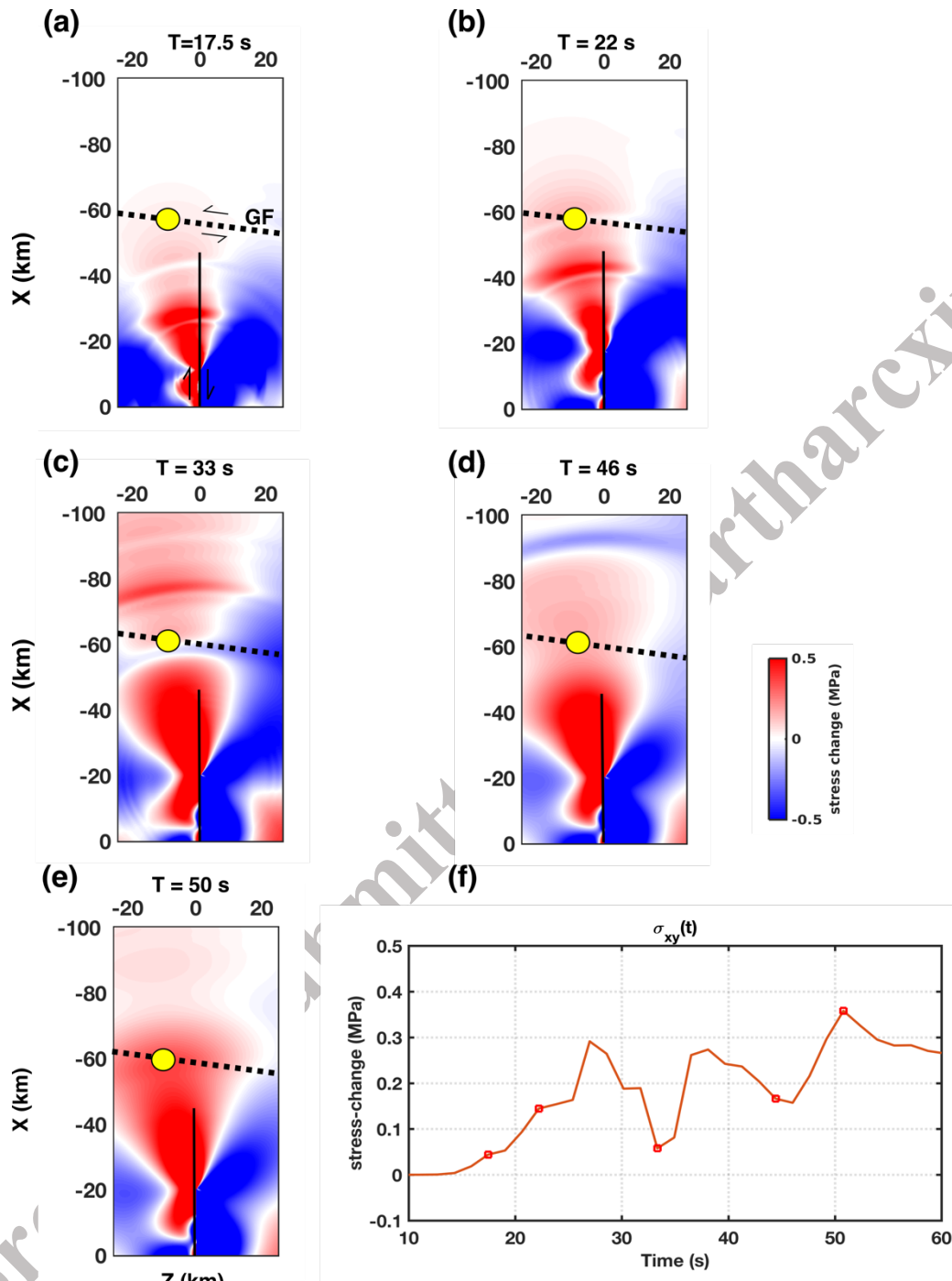
**Figure 8.** Similar to Fig. 9, but shear stress changes ($\sigma_{xy}$) during coseismic rupture. $\sigma_{xy}$ exhibits three distinct peaks in its temporal stress-change on the Garlock fault at ~28, 38, and 50 seconds. The color version of this figure is available only in the electronic edition.

(a)



(b)
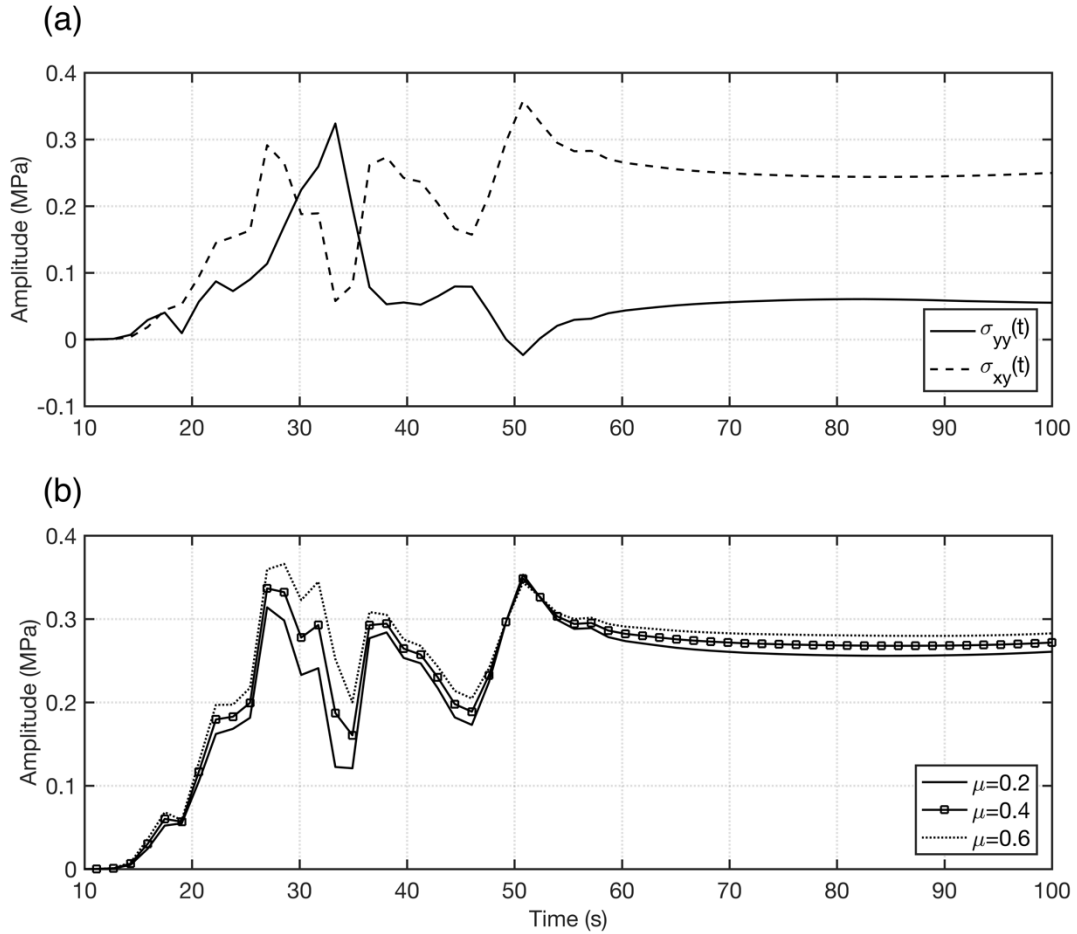
834
835 **Figure 9.** Stress change evolution on a section of the Garlock fault during the entire Ridgecrest
836 earthquake simulation. (a) Normal ($\sigma_{yy}$) and shear ($\sigma_{xy}$) stress change. (b) Temporal Coulomb
837 stress change for friction coefficient levels assessed in the static stress change analysis. Note that
838 we plot the temporal stress change starting at 10 seconds because this is when the nucleation
839 procedure ceases.